Dynamics and energy landscape of DNA plectoneme nucleation

Philipp U. Walker,[1] Willem Vanderlinden,[1,2] and Jan Lipfert[1,*]

[1]*Department of Physics, Nanosystems Initiative Munich, and Center for Nanoscience, LMU Munich,
Amalienstrasse 54, 80799 Munich, Germany*

[2]*Department of Chemistry, KU Leuven, Celestijnenlaan 200F, 3001 Heverlee, Belgium*

DNA buckling is the fundamental step for plectoneme nucleation and supercoil dynamics that are critical in the processing of genetic information. Here we systematically quantify DNA buckling dynamics using high-speed magnetic tweezers. Buckling times are $\sim$10–100 ms and depend exponentially on both applied force and twist. By deconvolving measured time traces with the instrument response, we reconstruct full two-dimensional extension-twist energy landscapes of the buckling transition that reveal an asymmetry between the pre- and postbuckling states and suggest a highly bent transition state conformation.

I. INTRODUCTION

DNA stores genetic information as a linear sequence and consequently needs to be very long. To achieve compaction in the narrow confines of the cell, while providing local accessibility for readout and processing, genome architecture is dynamically controlled [1–4]. Regulation is achieved by organizing DNA into domains, wherein DNA rotational motion is constrained. As a result, the number of links between the two single strands of the double helix, called the linking number Lk, is invariant. The topological quantity Lk partitions into the geometric parameters twist Tw and writhe Wr [5,6],

$$Lk = Tw + Wr, \tag{1}$$

where Tw quantifies the torsional deformations and strains of the helix, and Wr quantifies the coiling of the double-helix axis in three dimensions. Specialized proteins maintain cellular DNA in a supercoiled state, i.e., Lk deviates from the torsionally relaxed value Lk^0 *in vivo*. Through topological coupling, the linking difference $\Delta Lk = Lk - Lk^0$ affects DNA structure both locally and globally, via changes in twist ΔTw and writhe ΔWr, respectively [3,7,8]. Supercoiled DNA *in vivo*, in general, is both untwisted and takes on interwound, plectonemic configurations of the double-helix axis. The structure and mechanics of plectonemic DNA have been probed extensively by electron and atomic force microscopy of circular DNA molecules and by measurements of DNA tethered between a surface and magnetic beads in magnetic tweezers (MTs) [Fig. 1(a)] [9–11]. In contrast, the dynamics of plectonemes remain largely unexplored, despite their importance in the context of regulation and long-range communication in the cell [12].

A first direct measurement of plectoneme dynamics by fluorescence imaging [13] found that, within the time resolution of the approach (20 ms), a plectoneme can disappear at one

site and give rise to the appearance of a new plectoneme separated by several microns along the chain. The dynamics of this process are proposed to be rate-limited by nucleation of the newly formed plectoneme, i.e., by DNA buckling, in particular since removal of the plectoneme has been shown to be very fast [14]. Estimates for the characteristic time scale of DNA buckling range from 30 to 80 ms in MTs [11,15], to $\sim$100 ms in an optical torque wrench [16,17], and they are, surprisingly, approximately two orders of magnitude faster than for double-stranded RNA [15]. However, a direct comparison of the different measurements is complicated as the dynamics depend on ionic strength and applied stretching force. The lack of a precise quantitation of DNA buckling dynamics is due at least in part to the difficulty of observing fast $\sim$ms timescale transitions using camera-based detection.

Here, we have used high-speed MTs to quantify the kinetics of supercoil nucleation under a range of forces, ionic strength, and bead sizes. Using a deconvolution approach, we reconstruct the two-dimensional (2D) energy landscape of the buckling transition as a function of DNA extension and twist. We propose a geometric model for the transition state and discuss how local disturbances of the helix can impact the energy landscape of supercoiling.

II. RESULTS AND DISCUSSION

A. Bead tracking with kHz time resolution accurately quantifies DNA buckling transitions

In our MTs setup, linear $\sim$7.9 kbp DNA molecules are tethered between the flow cell surface and superparamagnetic beads, via multiple attachment points at both ends to assure torsionally constrained attachment [Fig. 1(a) and Sec. IV]. We note that our DNA length approximately corresponds to the size of topological DNA domains *in vivo*, $\sim$10 kbp [18]. Using external magnets, one can apply precisely calibrated forces [10,19,20] and control the linking number of the DNA. On increasing ΔLk at forces < 6 pN [21], DNA undergoes a buckling transition and starts to form plectonemes, causing a decrease in the apparent tether extension with increasing

───────
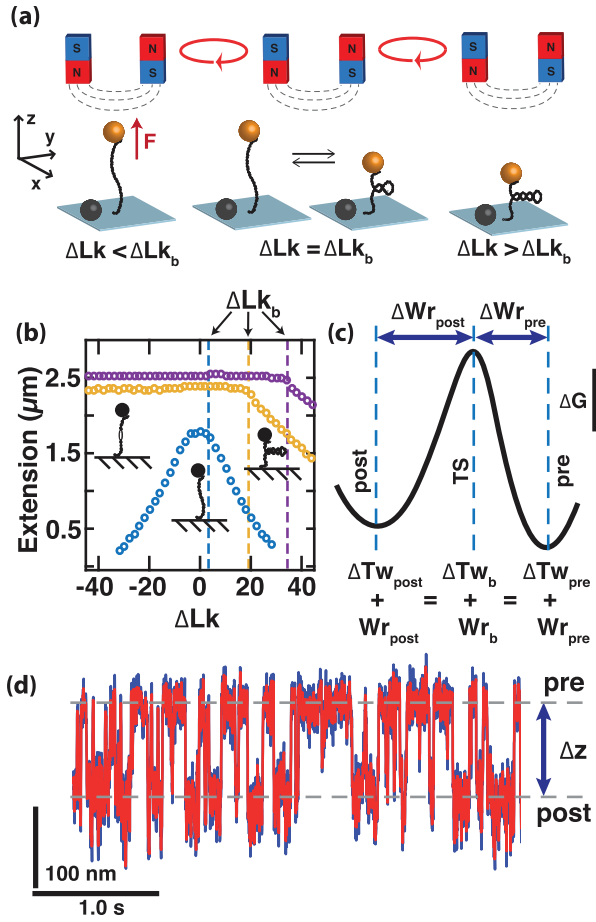*Author to whom all correspondence should be addressed: jan.lipfert@lmu.de

FIG. 1. DNA buckling measurements in the MT. (a) Schematic of the MT setup. A DNA molecule is tethered between the surface and a superparamagnetic bead. Magnets exert a force on the bead, and the rotation of the magnets controls the linking number. Close to the buckling point ΔLk_b, the DNA extension jumps between two states. (b) Rotation-extension curves for different forces. At low forces (blue, 0.2 pN) DNA forms plectonemes at positive and negative turns. At higher forces (yellow, 2 pN; purple, 5 pN) plectonemes appear only at positive turns, while DNA melts at negative ΔLk. (c) Schematic representation of the buckling energy landscape along the rotational coordinate at ΔLk_b. (d) Extension trace close to ΔLk_b, depicting the dynamic hopping of the DNA molecule between the prebuckling and postnucleation states. Δz indicates the jump size (raw data at 1000 Hz, blue; smoothed data at 333 Hz, red).

ΔLk [Fig. 1(b)]. If DNA molecules are held at a fixed ΔLk close to the buckling point ΔLk_b, the molecules undergo thermally activated transitions between the torsionally strained but extended prenucleation state, and the postnucleation state, with the first, minimal plectoneme formed [Fig. 1(c)]. Here, we draw on improvements in both camera and illumination hardware as well as tracking software [22–24] to study supercoil nucleation by tracking at 1 kHz in MT. Simulations show that our experimental configuration can resolve transitions on the time scale of ~ 10 ms or less, with an error of at most 10% [Fig. 1(d) and Fig. S1 in [25]]. In addition, from an analysis of experimental extension time traces of torsionally relaxed DNA tethers, we find the characteristic ("corner") frequencies at 2, 3, and 4 pN to be 98 ± 3, 161 ± 6, and $230 \pm$

12 Hz (means and standard errors from four independent measurements at each force), respectively, corresponding to characteristic time scales of 10, 6, and 4 ms, again suggesting that events on a time scale of ~ 10 ms can be detected (Fig. S2 in [25]).

B. Equilibrium properties of the DNA buckling transition

To quantify the extension time traces, we separate the extensions into two states by thresholding [26]. Upon stepwise increasing ΔLk, the time spent in the buckled state systematically increases at the expense of the population of the extended state [Fig. 2(a)]. We analyze our experimental data using a two-state model [11,26], where the energy difference between the pre- and postbuckling states is related to ΔLk, and the probability to be in the postbuckling state P_{post} is given by

$$P_{\text{post}} = \left(1 + e^{(2\pi)^2 (\frac{C}{L_C})(\Delta Lk_b - \Delta Lk)\Delta Wr_b/(k_B T)}\right)^{-1}, \quad (2)$$

where C is the effective torsional stiffness (approximated in the Moroz-Nelson model [27] or using data from direct torque measurements [28]; see [26]), L_C is the contour length, ΔLk_b is the buckling point, i.e., the number of applied turns for which $P_{\text{pre}} = P_{\text{post}}$, $\Delta Wr_b = Wr_{\text{post}} - Wr_{\text{pre}}$ is the number of turns converted from twist to writhe during buckling, k_B is the Boltzmann constant, and T is the temperature. Fitting of Eq. (2) to the experimentally observed P_{post} as a function of ΔLk yields ΔLk_b and ΔWr_b [Fig. 2(b)]. Over the force range investigated, ΔWr_b remains essentially constant [Fig. 2(c)], in agreement with previous experimental results for both DNA [11] and RNA [15]. We find that ΔWr_b increases by $\sim 33\%$ upon increasing the monovalent salt concentration from 100 to 320 mM, again in quantitative agreement with previous findings [11,15].

C. Kinetic analysis of DNA buckling

Having characterized the equilibrium properties of the buckling transition, we now focus on its dynamics, by analyzing the dwell times in the DNA extension traces. At each imposed ΔLk, the dwell time distributions for both the pre- and postbuckling state are well described by single exponential fits, which yield the mean lifetimes τ_{pre} and τ_{post} [Figs. 2(d) and 2(e)]. The lifetimes τ_{pre} and τ_{post} follow an Arrhenius relationship with an exponential dependence on ΔLk [Fig. 2(f)] [11]:

$$\tau_{\text{pre}} = \tau_{\text{buck}} e^{-(2\pi)^2 (\frac{C}{L_C})(\Delta Lk_b - \Delta Lk)\Delta Wr_{\text{pre}}/(k_B T)}, \quad (3)$$

where τ_{buck} is the lifetime at the midpoint of the buckling transition ΔLk_b, and ΔWr_{pre} is the change in writhe from the prebuckling state to the transition state. We used a similar expression for τ_{post} with ΔWr_{pre} replaced by $-\Delta Wr_{\text{post}}$, the rotational distance to the transition state from the postbuckling state [Fig. 1(c)].

Fits of Eq. (3) to τ_{pre} and τ_{post} were used to determine the characteristic buckling time τ_{buck} as well as ΔWr_{pre} and ΔWr_{post} [Fig. 2(g)]. The buckling time τ_{buck} increases with bead size, consistent with a model where the bead fluctuations are transmitted through the DNA molecule [29] (see Sec. II D below). For a fixed bead size, previous work [11] found a
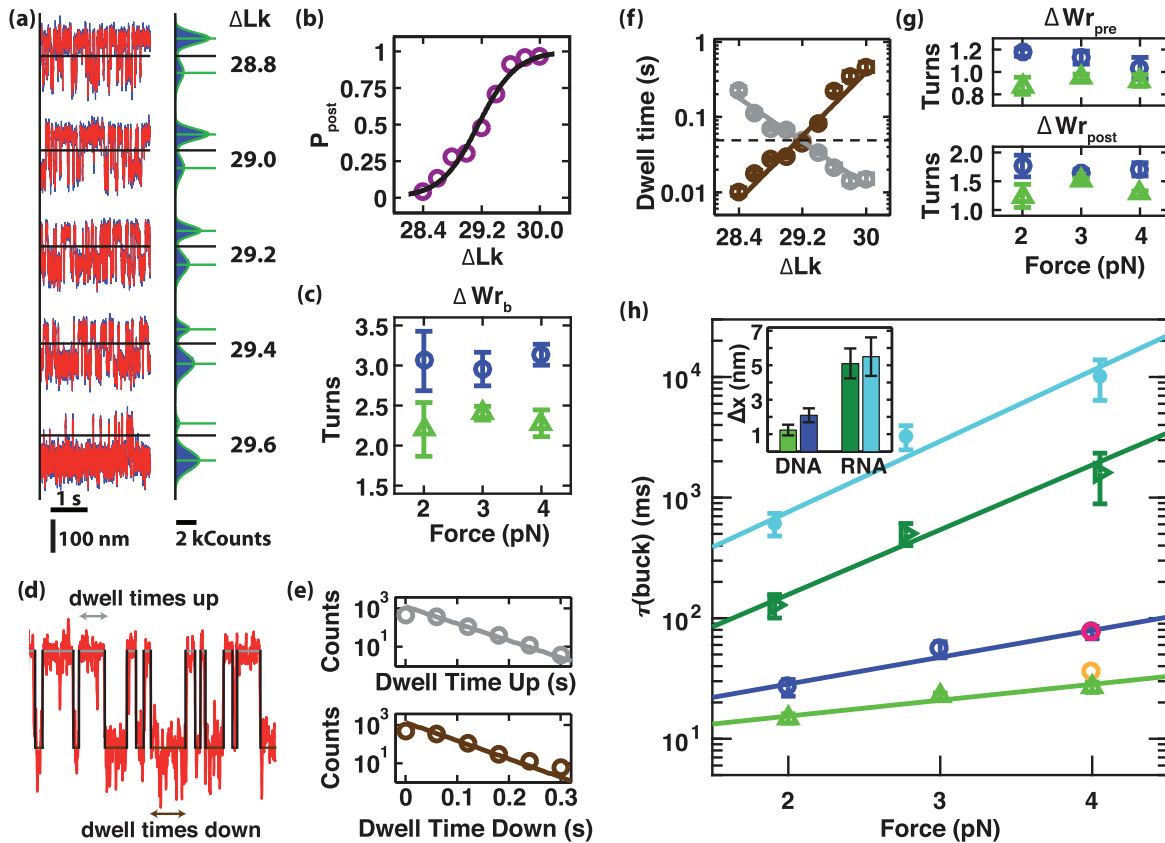
FIG. 2. Quantification of DNA buckling dynamics. (a) Extension time traces as a function of ΔLk (raw data 1000 Hz, blue; smoothed data 333 Hz, red). Black lines indicate thresholds for analysis. Histograms on the right are based on raw data and fitted by a double Gaussian. Horizontal green lines depict the mean extension of the pre- and postbuckling state, respectively. (b) Fraction in the postbuckling state vs ΔLk and fit of Eq. (2) (solid line) at 3 pN and 320 mM NaCl. (c) Salt and force dependence of ΔWr_b (green triangles 100 mM NaCl, blue circle 320 mM NaCl). (d) Example extension time trace indicating conversion of the filtered trace (red) into a binary signal (black) after selection of the threshold. Examples of dwell times in the pre- ("up") and postbuckling ("down") are indicated in the plot. (e) Example histograms and exponential fits (solid lines) of dwell times for constant ΔLk close to ΔLk_b (3 pN, 320 mM NaCl). (f) Mean dwell time for the pre- and postbuckling states vs ΔLk and fits of Eq. (3) (solid lines). The dashed line indicates the fitted buckling time τ_{buck}. (g) Distances to the transition state $|\Delta Wr_{\text{pre}}|$ and $|\Delta Wr_{\text{post}}|$ [same color code as in (c)]. (h) Buckling times vs force for DNA [bottom two data sets; same color code as panel (c)] and RNA (top two data sets; dark green right-pointing triangle data are for 100 mM and cyan dot data for 320 mM NaCl) for different salt concentrations and exponential fits [Eq. (4); solid lines]. Magenta and orange circles for 4 pN, 320 mM NaCl taken from Ref. [11] for 10.9 and 1.9 kbp DNA, respectively. Inset: distances to transition state Δx for DNA and RNA. All RNA data taken from [15].

weak dependence of the characteristic buckling time on DNA length (comparing 1.9 and 10.9 kbp DNA gave a difference of twofold in the buckling times); our data for 7.9 kbp DNA under the same conditions fall between the previous measured buckling times, as would be expected for the intermediate length [Fig. 2(h), differently colored points at 4 pN, 320 mM]. For a fixed bead size and DNA length, the characteristic buckling time τ_{buck} is strongly dependent on force F, and is well described by an exponential model [solid lines in Fig. 2(h), reduced $\chi^2 = 0.4$ and 0.3 for 100 and 320 mM NaCl, respectively]:

$$\tau_{\text{buck}} = \tau_{\text{buck},0} e^{F\Delta x/(k_B T)} \qquad (4)$$

with Δx the distance to the transition state and $\tau_{\text{buck},0}$ the buckling time in the absence of applied force. From a fit of Eq. (4), we obtain $\tau_{\text{buck},0}$ for DNA to be 8 ± 2 and 10 ± 3 ms [values and standard errors from the exponential fit, Fig. 2(h)] for 100 and 320 mM NaCl, respectively. These

values agree with one another, within experimental error, and are close to the extrapolated buckling times at zero force for RNA [15] ($\tau_{\text{buck},0} = 13 \pm 7$ and 52 ± 38 ms at 100 and 320 mM NaCl, respectively). The large differences between the buckling times τ_{buck} for DNA and RNA under tension can, therefore, primarily be attributed to differences in Δx, which are much smaller for DNA than for RNA under otherwise identical conditions [Fig. 2(h), inset], supporting our previous hypothesis that the striking difference in the buckling dynamic between DNA and RNA is mostly driven by differences in the transition state. We note that supercoil nucleation does not merely depend on force, but on torque as well [the different points in Fig. 2(h) are not only at different forces, but also at different torques, since the buckling point ΔLk_b shifts significantly with applied force]. Therefore, Δx is a value that quantifies the position of the energy barrier in a simplified 1D representation of the energy landscape. Its value does not directly reflect a physical position of the transition state, but
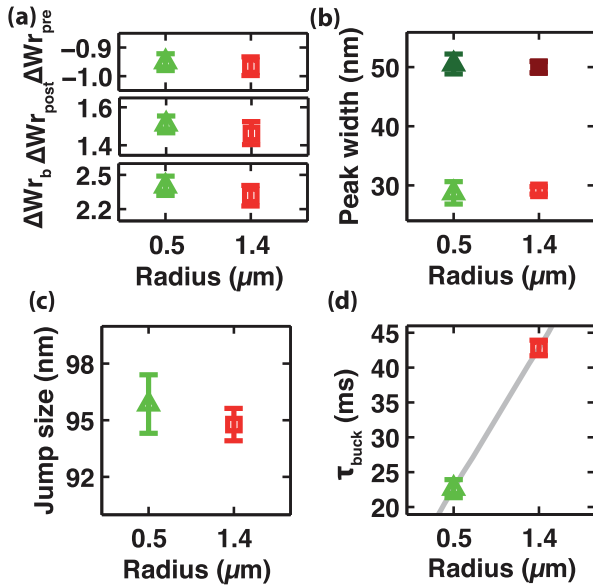
FIG. 3. Influence of bead size on DNA buckling transitions. (a) Effect of bead size on rotational distance to the transition state. For ΔWr_{pre}, ΔWr_{post}, and ΔWr_b no dependence on bead size is observed. (b) Influence of bead size on the widths of the pre- and postbuckling peaks in the extension histograms. The peak widths of the pre- as well as of the postbuckling state show no dependence on bead size (bright empty symbols, prebuckling state; dark filled symbols, postbuckling state). (c) Effect of bead size on the size of the jump, i.e., on the distance along the extension coordinate between the pre- and postbuckling states. For the jump size, no influence of the bead size can be observed. (d) Effect of bead size on characteristic buckling times τ_{buck}. An increase of the bead radius by a factor of 2.8 results in a change in the buckling time of $\sim$1.9-fold. All data shown are for 100 mM NaCl and 3 pN applied force; throughout, the green upward-pointing triangles are data obtained with MyOne beads, while red squares correspond to data recorded using M270 beads. See also Sec. II D.

should rather be interpreted as a characteristic length that describes the transition. A full description of the transition needs to consider the energy landscape along the rotational (twisting, writhing, and linking) and extension (DNA end-to-end distance) degrees of freedom (see Sec. II E below).

To quantify the energy landscape of supercoil nucleation along the rotational degree of freedom, we first determined the distances to the transition state from the prebuckling and postbuckling states ΔWr_{pre} and ΔWr_{post} from fits of Eq. (3) [Fig. 2(f)]. Both ΔWr_{pre} and ΔWr_{post} change systematically with salt concentration, but remain approximately constant with increasing force [Fig. 2(g)] and bead size (Fig. 3). Notably, ΔWr_{post} and ΔWr_{pre} add up to the measured value for ΔWr_b, within experimental error (Fig. S3 in [25]), as would be expected, since they are measured along the same coordinate. The ratio $\Delta Wr_{\text{pre}}/\Delta Wr_{\text{post}}$ is independent of force and ionic strength, within experimental error, and suggests the transition state along the writhing degree of freedom to be closer to the prebuckling state than the postbuckling plectonemic state ($|\Delta Wr_{\text{pre}}/\Delta Wr_{\text{post}}| = 0.68 \pm 0.05$ and 0.65 ± 0.03 for 100 and 320 mM NaCl, respectively). Since the transition occurs at a constant ΔLk, the measured ratio of

$|\Delta Wr_{\text{pre}}/\Delta Wr_{\text{post}}|$ implies that the transition state in the twisting degree of freedom is closer to the postbuckling state than the prebuckling state.

D. Influence of bead size on the properties of the buckling transition

Manipulation of individual molecules in single-molecule torque and twist assays requires the attachment of $\sim \mu$m-sized magnetic beads or nanofabricated cylinders to enable external control of the molecules [16,28,30]. Attachment of $\sim \mu$m-sized particles can affect the observed dynamics of conformational changes [14,29], as the attached particles influence both the friction coefficient and magnitude of the thermal fluctuations. To systematically test the influence of the bead size in our assay, we measured the dynamic as well as the steady-state properties for two different bead sizes for one set of conditions ($F = 3$ pN and a salt concentration of 100 mM NaCl). We used two different bead sizes, one with radius 0.5 μm and the other with a radius of 1.4 μm, hence the ratio of the bead sizes is 2.8.

We find that the equilibrium properties of the buckling transition are not affected by bead size. The angular distance to the transition state from the prebuckling state ΔWr_{pre}, as well as from the postbuckling state ΔWr_{post}, and the amount of twist converted into writhe ΔWr_b do not change within measurement error [Fig. 3(a)]. Consequently, also for the larger beads ΔWr_{pre} and ΔWr_{post} add up to ΔWr_b and show the same asymmetry as for the smaller bead results presented above [Figs. 3(a) and Figs. 2(c) and 2(g)]. Furthermore, the widths of the peaks in the extension histograms corresponding to the pre- and postbuckling states do not show any dependence on bead size [Fig. 3(b)]. Similarly, the total size of the extension jump between the pre- and postbuckling states is independent, within error, of bead size: we find a jump size of $(94.8 \pm 0.9 \text{ nm})$ for the 1.4 μm beads $(95.9 \pm 1.6 \text{ nm})$ for the smaller 0.5 μm radius beads [Fig. 3(c)].

In contrast to the static properties, the buckling times change significantly with bead size. For 3 pN, 100 mM NaCl we measured a characteristic buckling time of 22.7 ± 1.3 ms for 0.5 μm beads and 42.8 ± 1.1 ms for 1.4 μm beads [Fig. 3(d)]. We note that the observed differences in buckling times are not due to a lack of spatiotemporal resolution of the instrumental setup. Our simulations (see Sec. IV G) demonstrate that different bead sizes of 0.5 and 1.4 μm radius give rise to deviations due to limited spatiotemporal resolution of less than 5% for the observed buckling times and cannot explain the observed difference.

To understand the effect of the bead size on the buckling times, we consider the model by Bai *et al.* [29]. Briefly, due to the slower fluctuations of the bead compared to the DNA conformational fluctuations, bead-induced fluctuations in tension and twist are transmitted through the DNA molecule. The rate of energy barrier crossing events depends on the attempt frequency, which in turn is influenced by the viscous drag of the bead and the DNA molecule. Therefore, at a given constant force, the characteristic dwell time before a thermally driven barrier crossing event is given by

$$\tau = \frac{\varsigma_{\text{bead}} + \varsigma_{\text{DNA}}}{k_{\text{DNA}}} e^{\frac{\Delta G}{k_B T}}, \tag{5}$$

where the drag coefficient of the bead is $\varsigma_{bead} = 6\pi\eta R$ with η the viscosity of the solution and R the bead radius, $\varsigma_{DNA} = 2\pi\eta z/\ln(z/b)$ is the drag coefficient of the DNA [31] with z the extension of the DNA and $b = 2\,\mathrm{nm}$ the DNA thickness, k_{DNA} is the spring constant of the DNA, and ΔG is the energy barrier. At constant force, the—generally force-dependent—property k_{DNA} can be assumed to be a constant [29]. The ratio of our measured values [Fig. 3(d)] is $\tau_{buck}(R_{large})/\tau_{buck}(R_{small}) = 1.9 \pm 0.1$, which is smaller, but close to the prediction from the model of Bai *et al.* [Eq. (5)] of ≈ 2.4. This deviation might be partially due to the fact that fluctuations and the plectonemic loop increase the DNA friction term compared to the model's assumption of a simple elongated cylinder. Taken together, the data strongly suggest that the observed dependence of buckling times on bead size is due to coupling of the Brownian dynamics of the bead through the DNA, which sets the intrinsic frequency of barrier crossing attempts. Together with the results of our simulations, we conclude that the bead strongly influences the attempt frequency to cross the energy barrier, but that we do not fail to observe buckling transitions due to limited spatiotemporal resolution.

E. Energy landscape reconstruction at buckling equilibrium

To obtain a full quantitative description of the buckling transition and to account for its mutual dependence on extension and rotation, we reconstructed the 2D free-energy landscape $\Delta G(z, \Delta Lk)$. At a given ΔLk, $\Delta G(z) = -k_B T \ln[p(z)]$ with the probability density $p(z)$ [32]. To account for the effect of the force probe, we deconvolved the extension histogram of the DNA tether with the setup response function $S(z)$ [32–35]. For the deconvolution procedure, we used the bead fluctuations of torsional unconstrained DNA molecules at the same force and buffer conditions as the instrument response function (Fig. 4 and Sec. IV). The deconvolution sharpens the extension histogram [Fig. 4(a)], which is then converted to the corresponding 1D energy landscape to enable the analysis of the buckling transition along the extension coordinate. We compared the energy landscape obtained by deconvolution to the energy barrier reconstructed by a different approach, based on the splitting probability [36,37] with no need for deconvolution [35], and we obtained good agreement between the two methods [Fig. 4(b) and Sec. IV]. Finally, by assembling a series of 1D extension energy landscapes while systematically varying ΔLk we reconstruct the full 2D extension-linking number energy landscape; see below.

We analyze the reconstructed energy landscape focusing on the extension coordinate at ΔLk_b, i.e., at the point where the forward and backward rates are equal [26]. At ΔLk_b, the distances to the transition state along the extension coordinate from the pre- and postbuckling state minima, Δz_{pre} and Δz_{post}, were found to be dissimilar, independent of force [Fig. 4(d) and Fig. S4 in [25]]. The values suggest that the transition state along the extension coordinate is closer to the pre- than to the postbuckling state [Fig. 4(d)]. Notably, Δz_{pre} and Δz_{post} add up to the total jump size as determined directly from extension distributions (Fig. 5). At ΔLk_b, the reconstructed energy landscape [Figs. 4(b) and 5(b)] shows a broader energy minimum for the postbuckling state compared
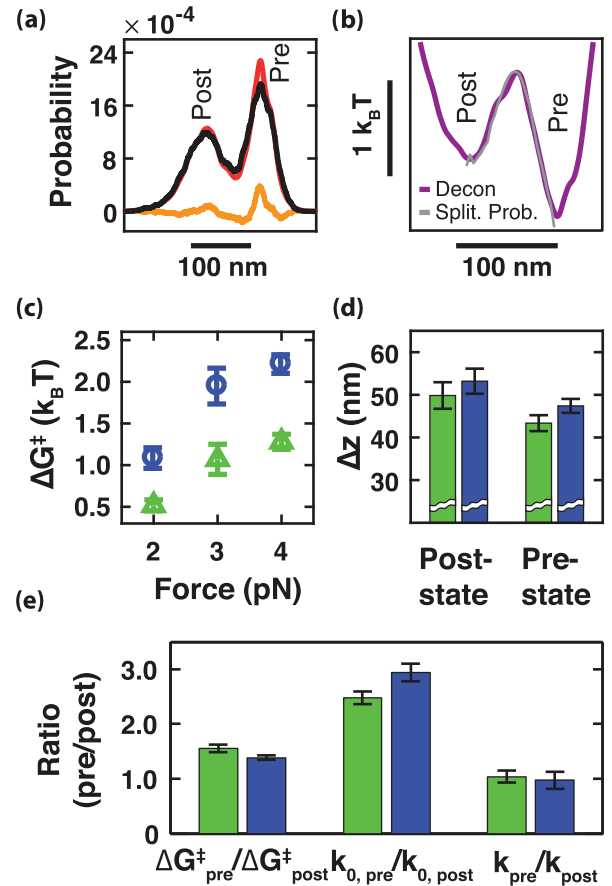

FIG. 4. Reconstruction and quantification of the energy landscape. (a) Deconvolution of extension histograms. Extension histogram before (black) and after (red) deconvolution with the setup response function and difference due to deconvolution (orange). (b) Reconstructed energy landscape computed as $\Delta G(z) = -k_B T \ln[p(z)]$ from the deconvolved probability density $p(z)$ (purple) as well as with the underlying splitting probability (gray). (c) Mean value of the energy barrier at ΔLk_b of the pre- and postbuckling state vs force [color code for panels (c)–(e): 100 mM NaCl, green and 320 mM NaCl, blue]. (d) Distances to the energy barrier along the extension coordinate (absolute values). (e) Comparison of post- and prebuckling state parameters at ΔLk_b: The energy barrier for the prebuckling state $\Delta G^{\ddagger}_{pre}$ is larger than for the postbuckling state $DG^{\ddagger}_{post}$ resulting in $\Delta G^{\ddagger}_{pre}/\Delta G^{\ddagger}_{post} > 1$. The ratio of the attempt frequency of the bead to cross the energy barrier of the prebuckling state by the postbuckling state $k_{0,pre}/k_{0,post}$ determined by the ratio of the curvature of the energy landscape is larger than 1. The overall rate to cross the energy barrier $k_{pre}/k_{post} \approx 1$ in line with equilibrium at ΔLk_b.

to the prebuckling state, corresponding to a larger conformational space after buckling. The broader energy minimum after buckling corresponds to a smaller curvature (Fig. 6) and, applying Kramers theory [33,38,39], to a smaller attempt rate k_0 for barrier crossing at buckling equilibrium compared to the prebuckling state. Since the forward and backward rates are identical at ΔLk_b, the difference in k_0 is compensated by different barrier heights $\Delta G^{\ddagger}_{pre}$ and $\Delta G^{\ddagger}_{post}$ [Fig. 6 and Figs. S4(c) and S4(f) in [25]] measured from either side of the transition state. We conclude that the energy barrier, measured
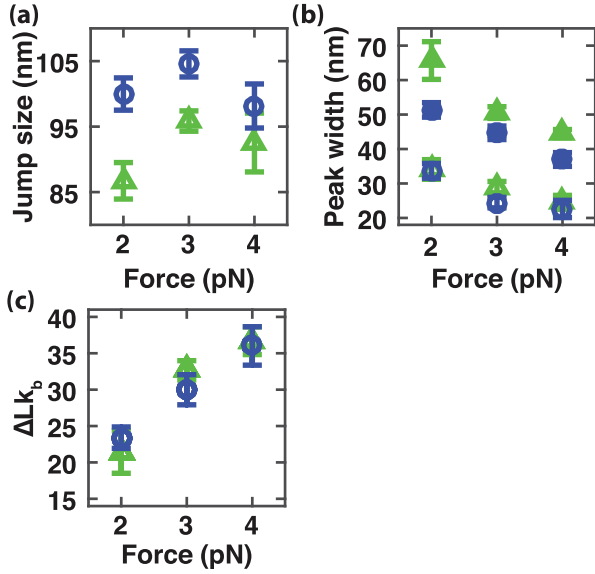
FIG. 5. Equilibrium properties of the buckling transition for DNA. (a) Sizes of the jump between the pre- and postbuckling states vs force for 100 and 320 mM NaCl. The jump size within one salt concentration stays nearly constant for the investigated forces. A larger jump size of 100.9 ± 4.6 nm for 320 mM NaCl compared to the 91.7 ± 5.5 nm for 100 mM NaCl indicates a salt dependency. The sum of Δz_{pre} and Δz_{post} for 100 mM NaCl is 93.2 ± 3.6 nm and thus in good agreement with the directly determined jump size. For 320 mM NaCl, Δz_{pre} and Δz_{post} sum up to 100.6 ± 3.4 nm and consequently fit also to the jump size. (b) Widths of the peak of the pre- and postbuckling states in the extension histograms. For both salt concentrations, the peak width of the Gaussian-distributed histograms for the postbuckling state (filled symbols) is significantly larger than the peak width of the prebuckling state (empty symbols). In all cases, the peak width decreases with increasing force. For the prebuckling state at one given force, no or only a small salt dependency is observed, while for the postbuckling state the error bars do not overlap. (c) Number of twists applied at the buckling point ΔLk_b vs force. ΔLk_b increases with force, but does not depend on salt. Color code as in Fig. 2.
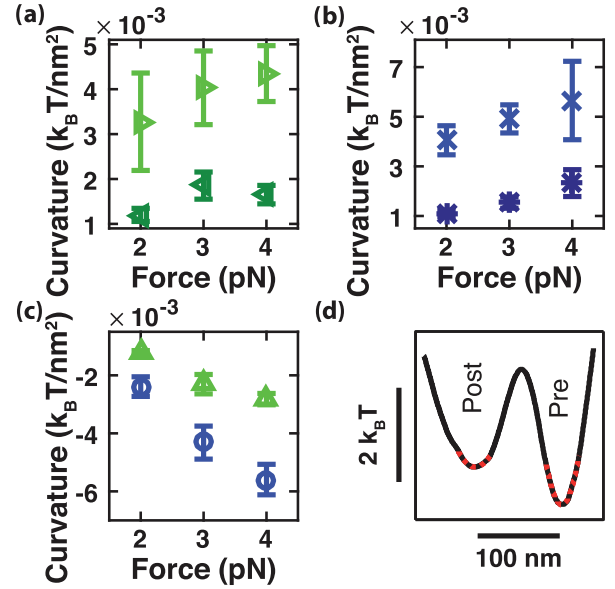

FIG. 6. Curvature of the reconstructed energy minima and maxima. (a) Curvature of energy valleys at 100 mM NaCl. No significant trend in force is observed, neither for the prebuckling state (green right-pointing triangle) nor for the postbuckling state (dark green left-pointing triangle). The curvature of the prebuckling state is always larger than for the postbuckling state. (b) Curvature of energy valleys at 320 mM NaCl. Again, no significant change in the curvature for all forces is obtained (blue cross: prebuckling state, dark blue asterisk: postbuckling state). As determined in panel (a), the curvature of the postbuckling state is smaller than for the prebuckling state. (c) Curvature of the energy barrier top. The absolute value of the curvature for 100 mM NaCl (green upward-pointing triangle) is for every force probed smaller than for 320 mM NaCl (blue circle). For both salt concentrations, a trend to higher absolute values of curvature at higher forces is observed. This is in qualitative agreement with the higher energy barrier at higher forces but force-independent curvature of the energy valleys and roughly constant jump size over all forces. (d) Curvatures were determined by a quadratic fit (dotted red line) around the minima of the wells that included the extension range of ± 20 nm around the minimum.

along the extension coordinate, is significantly asymmetric and steeper for buckling as for plectoneme removal.

The reconstructed energy landscape enables, in addition, the calculation of diffusion coefficients for barrier crossing, again from Kramers theory [see, e.g., Eq. (10) from Ref. [33]]. We find diffusion coefficients $D \approx 10^{-15}$ m^2/s, whereby the diffusion constants for the pre- and postbuckling wells agree essentially within error, but are slightly force- and salt-dependent. Values of $D \approx 10^{-15}$ m^2/s are in the same order of magnitude as reported for protein relaxation times and refolding landscapes [40,41] and smaller than DNA hairpin diffusion coefficients [33]. The determined diffusion coefficient of 10^{-15} m^2/s implies significantly slower diffusion than the translational diffusion of $\sim 1\,\mu$m beads, for which we estimate $D \approx (4–5) \times 10^{-13}$ m^2/s from the Einstein-Stokes relationship (even if accounting for the proximity of the surface [42,43]) in good agreement with experimental observations [44]. The diffusive bead motion in turn is slower than the purely translational diffusion of DNA with lengths

corresponding to the loop size, which is in the range of $\sim 10^{-11}$–10^{-12} m^2/s [45], also in agreement with experimental observations [14]. Thus, diffusive barrier crossing is several orders of magnitude slower than simple translational diffusion, which in turn implies substantial internal friction in the DNA as it evolves to the transition state. In line with a substantial amount of internal friction, the smaller impact on the bead size (Fig. 3) as well as on the viscosity of the buffer (Fig. S5 of [25]) as would be expected from Eq. (5) can be attributed to an internal friction that adds an additional term independent of the radius of the bead or the viscosity of the buffer.

The energy landscape reconstruction is not limited to the extension coordinate (Fig. 4); we can also quantitatively describe the energy landscapes along the rotational degree of freedom [Fig. 7(a)]. Using the values for $\Delta W r_{post}$ and $\Delta W r_{pre}$ [Fig. 2(g)] to determine the relative position along the writhe coordinate and the free-energy barrier heights from the energy
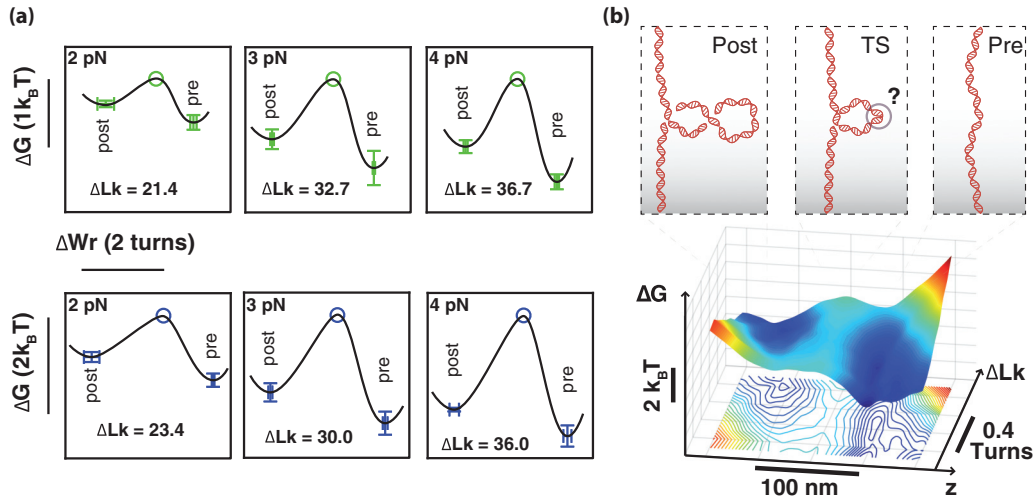
FIG. 7. Energy landscape of the DNA buckling transition. (a) Quantitative energy landscape along ΔWr for different forces and salt concentrations (upper row 100 mM NaCl, lower row 320 mM NaCl). Green and blue markers are determined from the analysis described in the main text. The energy landscape flattens for lower forces. Since the analysis only provides energy differences, the tops of the barriers are set to equal height for ease of comparison. (b) A full 2D extension and rotation energy landscape was obtained by subsequently constructing 1D extension energy landscapes (as in Fig. 4) while systematically changing ΔLk (in steps of 0.1 turns). The isoenergy lines in the projection of the landscape into two dimensions have a spacing of $0.15\,k_B T$. The asymmetry of the pre- and postbuckling energy wells is apparent.

landscape [Figs. S4(c) and S4(f) in [25]], we obtain a free-energy landscape along the ΔWr coordinate at fixed ΔLk_b that again reveals an asymmetrical distance to the transition state. The energy barrier flattens with decreasing force (see also Fig. S4 in [25]) in line with previous observations for force-dependent energy barriers [46]. By combining a series of 1D extension energy landscapes upon systematically varying ΔLk, we reconstruct the full 2D extension-linking number energy landscape [Fig. 7(b)].

III. CONCLUSION

In summary, taking advantage of the ability of MTs to control both the applied force and twist, we have reconstructed the full 2D energy landscape along the extension and twist degrees of freedom. Along the rotational degree of freedom, the energy landscape is asymmetric, with ΔWr_{pre} close to unity, and roughly 30% smaller as compared to $\Delta Wr_{\mathrm{post}}$. Likewise, the energy landscape along the extension coordinate exhibits significant asymmetry, with the distance from the extended to the transition state Δz_{pre} approximately 15% smaller than the distance from the buckled to the transition state Δz_{post}. Combining both results, we conclude that the transition state is a small, highly twisted single loop.

We hypothesize that the strong bending and twisting deformations in the transition state for DNA buckling lead to a breakdown of isotropic elasticity and result in the formation of a kinked loop [47]. A breakdown of harmonic elasticity for DNA could explain the finding from the force dependence of τ_{buck} that the buckling transition exhibits a threefold to fourfold steeper energy barrier for DNA as compared to RNA [Fig. 2(h)]. Barrier steepness quantifies the cooperativity of molecular rearrangements to achieve the transition state geometry; since the (harmonic) elasticity properties of both

nucleic acids are roughly the same, it is plausible that the transition involves the breakdown of DNA harmonic elasticity. This hypothesis is further supported by the observation that factors that destabilize double-stranded DNA, notably glycerol or low salt concentrations (Fig. S5 in [25]), increase the rate of buckling, consistent with a lower transition state energy barrier. Disruption of DNA base pairing upon negative supercoiling under stretching forces has been clearly established previously [48,49]. Our hypothesis of kinking and local disruption of base pairing is in line with biochemical and structural experimental results [50] and with all-atom molecular-dynamics simulations of small DNA circles [51] that indicate the formation of local kinks also upon positive supercoiling.

Our findings suggest that local defects [11,52], e.g., introduced by DNA damage or protein-binding [53], would enhance the rate of supercoil nucleation by transition state stabilization, and help positioning plectonemes. The rates of supercoil position hopping, previously determined using identical beads [13], are similar to the rates of supercoil nucleation determined in this study, which strongly suggests that long-range communication along DNA is rate-limited by supercoil nucleation. In summary, the quantitative framework presented here will enable us to make testable predictions of DNA topology-mediated regulatory dynamics and provides a critical baseline for models of DNA dynamics *in vivo*. In addition, our work highlights the necessity to decouple the energy landscape of supercoil nucleation along both extension and rotational degrees of freedom, and demonstrates how high-speed magnetic tweezers experiments allow reconstruction of full 2D free-energy landscapes, which opens up exciting possibilities to extend the more commonly used 1D free-energy description of macromolecular transitions [54] into multiple dimensions [55].

IV. MATERIALS AND METHODS

A. DNA constructs and magnetic beads

Measurements employed a 7.9-kbp DNA construct described previously [28,56]. For specific attachment to both the magnetic bead and the flow cell surface, ∼600-bp PCR-generated DNA fragments labeled with multiple biotin and digoxigenin groups, respectively, were ligated to the DNA. Measurements used either 1.0-µm-diameter MyOne or 2.8-µm-diameter M270 magnetic beads (Life Technologies, USA). The DNA construct was attached to the streptavidin coated beads by incubating 1 µL of picomolar DNA stock solution and 2 µL MyOne beads in 10 µL 1× PBS (Sigma-Aldrich, USA) for 12 min. Subsequently, 500 µL 1× PBS was added to get the final bead concentration, and the bead-coupled DNA constructs were introduced into the flow cell; see below. Alternatively, 0.5 µL DNA stock solution, 5.5 µL M270 beads were incubated in 20 µL 1× PBS for 8 min and diluted into 150 µL 1× PBS.

B. MT setup

The custom-built MT setup uses a pair of $5 \times 5 \times 5$ mm^3 permanent magnets (W-05-N50-G, Supermagnete, Switzerland), oriented in a horizontal configuration [19]. The distance between beads and magnets is controlled by a DC-Motor (M-126.PD2, PI, Germany), while rotation of the magnets is performed by another DC-Motor (C-150.PD, PI, Germany). Beads are observed with a 40× oil immersion objective (UPLFLN 40×, Olympus, Japan) and imaged with a CMOS sensor camera (12M Falcon2, Teledyne Dalsa, Canada). Reducing the field of view to 5% of the original area (to 1792×282 pixels, with 1 pixel ≈ 110 nm) enables a frame rate of 1 kHz. Images are transferred to a frame grabber (PCIe 1433, NI, USA) and analyzed with a custom-written tracking software [57]. A simple LED (69647, Lumitronix LED Technik GmbH, Germany) is used for illumination. A piezo stage (Pifoc P-726.1CD, PI, Germany) moves the objective to produce the look-up table (LUT) necessary for the bead tracking. Forces were calibrated as described by Te Velthuis *et al.* [58].

C. Flow cells and measurement buffers

Flow cells are built of two coverslips (24×60 mm, Carl Roth, Germany). The bottom coverslip, to which the DNA molecules will attach, is first coated with (3-Glycidoxypropyl)trimethoxysilane (abcr GmbH, Germany). Afterwards, 200 µL of a 2000 times diluted stock solution of polystyrene beads (Polysciences, USA) in ethanol (Carl Roth, Germany) is dried in air and baked at 100 °C for 5 min as reference beads. The two coverslips are glued together by one layer of melted Parafilm (Carl Roth, Germany), precut to form a flow channel. 100 µg/mL anti-digoxigenin (Roche, Switzerland) in 1× PBS are incubated in the assembled flow cell for 1 h. To minimize nonspecific interactions, the flow cell is flushed with 800 µL of 10 mg/mL bovine serum albumin (BSA) (Carl Roth, Germany), incubated for 1 h, and rinsed with 1 mL of 1× PBS. The premixed DNA-bead solution is added to the flow cell for 12 min for MyOne beads, and 7 min for M270 beads to allow for the digoxigenin–anti-digoxigenin

bonds to the surface to form. Subsequently, the flow cell is rinsed with 1 mL of 1× PBS to flush out unbound beads. The buffer was exchanged to the final measurement buffers by flushing 2 mL of buffer while applying 5 pN. Measurements were performed in Tris-EDTA buffer (TE) (Sigma-Aldrich, USA) containing 10 mM Tris-HCl and 1 mM EDTA at a pH of 8.0, with varying amounts of NaCl added, as indicated in the text. For some experiments, glycerol (Sigma-Aldrich, USA) was included in the buffer as noted in the relevant section.

D. Measurement protocol to detect the buckling transition

For every molecule included in the analysis, two initial tests were performed to test whether beads are attached via single double-stranded DNA tethers. First, the length of the tether was determined by applying a stretching force of 5 pN. Tethers within 10% of the expected length (assuming a contour length of the molecule equal to 0.34 nm/bp × 7900 bp ∼ 2700 nm and taking into account the WLC-like stretching response [59]) were considered for further analysis. To test whether DNA tethers were free of nicks and suitable for supercoiling experiments as well as to exclude beads attached to the surface via multiple DNA molecules, extension-rotation curves at 5 pN as well as at 1 pN were measured. Only beads behaving as in Fig. 1(b) (no length change at 5 pN within ±30 turns, asymmetric extension trace at 1 pN) were used for experiments. The torsionally relaxed position of the DNA molecule was determined by a rotation curve at 0.4 pN.

The buckling point of the DNA molecule was determined by rotating the molecule in positive turns until a clear jump in the extension is visible. Buckling transition measurements started around one turn before jumps and ended around one turn after jumps in the extension trace were observed. Traces were recorded for each number of applied magnet rotations for 100 s and the number of rotations was systematically varied in steps of 0.1 turns [Fig. 2(a)]. Unless otherwise noted, for all reported points at least four molecules were measured. All errors given are standard errors of the mean.

E. Analysis of hopping traces

Extension-time traces were recorded at 1 kHz and smoothed with a moving average filter of 3 ms. Control calculations with filter times in the range of 3–9 ms gave identical results, within experimental error (see also Sec. IV H). Data analysis was performed similar to Ref. [15]. In brief, an optimal threshold for separating the pre- and postbuckling state was determined by using 100 equally separated "trial thresholds" between the minimum and maximum extension value. The maximum of the first derivative of the fraction in the prebuckling ("up") state with respect to the threshold position was used as the optimal threshold. To avoid artifacts due to the tails of the extension histogram where the derivative of the fraction in the prebuckling is also close to zero, only the thresholds between the two peaks of the double-Gaussian-shaped extension histogram were considered as candidates for the optimal threshold. Control calculations were carried out by randomly changing the threshold position by up to 5% of the maximal difference in the z trace; the resulting change in the characteristic buckling time was less than 10%, suggesting

that our results are insensitive to the exact position of the threshold.

Extension traces were divided into pre- and postbuckled states by the optimal threshold. Time points of the jumps from one state into the other were used to determine the dwell time distributions in the pre- and postbuckling states for all traces. The buckling time distributions were fitted with a single exponential using a maximum likelihood fit, resulting in the mean residence time for both states at every number of applied turns [Figs. 2(d) and 2(e)]. These τ_{pre}^* and τ_{post}^* values were corrected for the finite acquisition time due to the camera frequency and filter by applying a statistical correction method based on the moment equations for a two-state Markov model (see Sec. IV H) [60]. The corrected mean dwell times τ_{pre} and τ_{post} and their corresponding rotation number were used to determine the characteristic buckling time τ_{buck} [Fig. 2(h)].

The force dependency of the characteristic buckling time [Eq. (4) and Fig. 2(h)] was fitted using the standard χ^2-criterion and the fitnlm function in MATLAB (MATLAB R2013b, The MathWorks), i.e., using $1/\sigma^2$ with σ the standard deviation as weighting factors. The reported errors for $\tau_{\mathrm{buck,0}}$ and Δx are the standard errors of the estimate.

F. Two-state model of the buckling transition

To quantify the different extension plateaus of the DNA molecules, we used the two-state model by Brutzer *et al.* [11]. Briefly, the free energy of the DNA molecule related to the twist before the buckling point is given by

$$E_{\mathrm{pre}}(\Delta Lk) = \frac{1}{2} \frac{C}{L_C} (2\pi)^2 \Delta Lk^2, \tag{6}$$

where ΔLk is the number of applied turns, L_C is the contour length, and C is the effective torsional modulus in $k_B T$ nm [27]:

$$C = C_{\mathrm{mod}} \left(1 - \frac{C_{\mathrm{mod}}}{4 L_p \cdot k_B T} \left(\frac{k_B T}{L_p \cdot F} \right)^{0.5} \right) \tag{7}$$

with C_{mod} the DNA torsional modulus, F the applied force, and L_p the persistence length. We used $100 k_B T$ nm and 45 nm for C_{mod} and L_p, respectively. Using experimental data for the effective torsional modulus instead [28] did not significantly change the results of the fits of Eqs. (2) and (3) in the main text. After buckling, the free energy is given by

$$E_{\mathrm{post}}(\Delta Lk) = E_b + \frac{1}{2} \frac{C}{L_C} (2\pi)^2 (\Delta Lk - \Delta Wr_b)^2, \tag{8}$$

where E_b is the energetic penalty that must be overcome for the formation of the buckling structure and ΔWr_b is the number of turns converted from twist to writhe during buckling. Using Boltzmann statistics, the probability to be in the postbuckling state P_{post} is given by

$$P_{\mathrm{post}} = \frac{1}{1 + e^{\frac{E_{\mathrm{post}} - E_{\mathrm{pre}}}{k_B T}}}. \tag{9}$$

With the expressions for E_{pre} and E_{post} [Eqs. (6) and (8)], the probability can be rewritten as

$$P_{\mathrm{post}} = \frac{1}{1 + e^{\frac{C}{L_C} \cdot (2\pi)^2 \frac{(\Delta Lk_b - \Delta Lk)\Delta Wr_b}{k_B T}}}, \tag{10}$$

where ΔLk_b is the number of applied turns where $P_{\mathrm{pre}} = P_{\mathrm{post}}$, i.e., the point of buckling equilibrium. Fitting of Eq. (10) to the probability to be in the postbuckling state regarding the number of applied turns, we determined ΔLk_b as well as ΔWr_b [Fig. 2(b)].

We determined the mean dwell times in the pre- and postbuckling state from a maximum-likelihood fit of exponential distribution to the data [Figs. 2(d) and 2(e)]. To describe the dependence of the mean dwell times in the pre- and postbuckling states, τ_{pre} and τ_{post}, we assume an Arrhenius relationship with exponential dependence on the number of applied turns, resulting in Eq. (3) [11].

G. Simulations of the DNA-bead system in the MT

To test our ability to resolve fast transitions in the MT, we carried out numerical simulations of our measurement system: an ∼8 kbp DNA tether attached to a 0.5 or 1.4 μm radius bead. In the simulations, the Langevin equation for the bead motion was solved numerically following the approach of Burnham *et al.* [61], taking into account the viscous drag of the bead (with appropriate modifications due to the proximity of the flow cell surface [42,43], the magnetic force, which is constant for a given setting of the magnets [19], and the force exerted by the DNA, which is modeled using the WLC model [59]). To this basic simulation framework of a magnetic bead tethered in the MT, we add stochastic jumps in the tether extensions. The simulated jumps are instantaneous in the simulations and increase or decrease the tether extension by 100 nm (similar to the buckling transition observed for DNA). The simulated steps occur at a predefined rate [Fig. S1(a) [25]]. The simulation code includes the effect of the camera by averaging the simulated positions (calculated for every 0.01 ms) over subsequent time intervals corresponding to the frame rate of the camera (1 ms). Simulated time traces are subjected to the same dwell time analysis routines as the experimental data: traces are filtered with a moving average filter, a threshold is selected, and dwell time distributions are computed. The simulation only examines the 50-50 point that has identical dwell times in both states, thus no maximum-likelihood fits of exponential distributions are required to extract the corresponding apparent mean dwell times, and we report simply the mean dwell time values for the upper and the lower state. The fitted dwell times are compared to the dwell times used as inputs in the simulations [Fig. S1(b) [25]]. The results suggest that for our measurement parameters, stochastic jumps in the trace with a characteristic time down to ∼10 ms can be resolved with at most 10% error using MyOne (0.5 μm radius) beads. For M270 (1.4 μm radius), the time resolution is worse, but even for these larger beads, jumps with a time scale down to 20 ms can be resolved with less than 10% error.

H. Correction for finite acquisition times

Limited time resolution of the instrument as well as the need to filter the data slightly [Fig. 2(a)] could produce a bias in our measured values for τ_{pre}^* and τ_{post}^*, leading to biased values for τ_{buck}^*. For the simulated data, as well as for the measured data, we tested down-sampling with different

widths for a sliding average filter from 3 to 9 ms, which did not affect τ_{buck} within the error. Furthermore, we tested the effect of correcting for finite acquisition time by applying a statistical correction method based on the moment equations for a two-state Markov model [60]. In brief, the influence of the detection limit of time ξ (due to the camera frequency and the width of the filter) to the true, intrinsic values τ_{pre} and τ_{post} of the system resulting in the observed time values τ_{pre}^* and τ_{post}^* is corrected by numerically solving the two equations [60]:

$$\tau_{pre}^* = (\tau_{pre} + \tau_{post})e^{\frac{\xi}{\tau_{post}}} - \tau_{post}, \tag{11}$$

$$\tau_{post}^* = (\tau_{pre} + \tau_{post})e^{\frac{\xi}{\tau_{pre}}} - \tau_{pre}. \tag{12}$$

The resulting corrected values τ_{pre} and τ_{post} were slightly smaller than the uncorrected values, but within the error (Fig. S6 [25]). Consequently, τ_{buck} was not significantly smaller. The largest effect was determined to be at the fastest buckling conditions and changed the characteristic buckling time by 15%. All data shown are corrected values.

I. Deconvolution procedure

To reconstruct the energy landscape without the blur of setup noise, the extension histograms from the measured time traces at fixed numbers of rotation were deconvolved with the instrument response function. We followed the approach of Woodside *et al.* [32,33,35] and utilize the nonlinear iterative method of Jansson [34]:

$$\hat{o}^{(k+1)}(z) = \hat{o}^{(k)}(z) + r[\hat{o}^{(k)}(z)] \cdot (i(z) - S(z) \, x \, \hat{o}^{(k)}(z)),$$
$$r[\hat{o}^{(k)}(z)] = r_0 \cdot \left(1 - 2 \cdot \left|\hat{o}^{(k)}(z) - \frac{1}{2}\right|\right) \tag{13}$$

with $i(z)$ the measured histogram, $S(z)$ the setup noise, and $\hat{o}^k(z)$ the deconvolved histogram after k iterations. $r[\hat{o}^{(k)}(z)]$ is the function to remain within the physical boundaries with the constant r_0 to control the speed of convergence.

We first generated the extension histogram from the raw measurement trajectories. The z-traces were binned to 0.2 nm and the resulting histograms were smoothed with a moving average filter of a width of 4.2 nm. To reduce spurious fluctuations in the deconvolution, after every iteration the histograms were smoothed with a moving average filter of width 1.2 nm. For every measurement we performed 1000 iterations with $r_0 = 2$.

Woodside *et al.* deconvolved their measurements on DNA hairpins with the noise of the DNA handles in their optical trap determined with a hairpin that is always in a closed configuration. In our case, the DNA tether serves both as the handle as well as the system of interest itself. Hence, we cannot directly use the DNA handle with a modified version of the system of interest, which is always in one fixed configuration as the instrument response function to deconvolve the measurement. Instead, we use the extension fluctuations of torsionally relaxed molecules, which are well approximated by a Gaussian, as the instrument response function $S(z)$ (Fig. S7 [25]) [61]. To address the effect of force on the fluctuations, we measured

the extension fluctuations in the absence of supercoils for every force used in our analysis. Furthermore, the fluctuations of torsional unconstrained DNA molecules were determined for 100 and 320 mM NaCl buffers. The results are well described by a model based on the wormlike chain model for DNA (Fig. S7 [25]) and we did not observe a significant change in fluctuations depending on salt concentration. Nevertheless, all energy landscape reconstructions were performed with the characteristic setup noise of the corresponding force and buffer, approximated by Gaussian distributions with standard deviations ranging from $\sigma \sim 10$ to ~ 19 nm.

We note that the noise of the tracker (quantified by the standard deviation of the tracked z-position of the bead fixed to the surface) of $\sigma \sim 1$ nm is more than one order of magnitude smaller than the z-fluctuations of DNA-tethered beads. Therefore, the instrument response function $S(z)$ is dominated by the thermal fluctuations of the bead-DNA tether and not by the optical or tracking resolution. The deconvolution procedure resulted in stable solutions with small residuals and is robust against changes reasonable dimensions (e.g., a factor of 2 in every parameter). Using a kernel density estimate with MATLAB (MATLAB R2013b, MathWorks) instead of the histogram did not result in significant changes of the energy landscape.

J. Determination of the energy barrier from splitting probability analysis

As an alternative approach to our deconvolution analysis for the energy landscape reconstruction, we applied an independent method to determine the energy barrier following Manuel *et al.* [33]. In brief: The splitting probability $p_{buck}(z)$ measures the likelihood that the DNA goes into the buckled state as a function of its extension position z [36]. Therefore, $p_{buck}(z)$ is approximately 0 for the prebuckling state, ≈ 0.5 at the transition state, and ≈ 1 is the postbuckling state. The probability $p_{buck}(z)$ can be directly determined from the measured trajectory of finite duration T for a given value of z_0:

$$p_{buck}(z_0) = \int_0^T \delta(z_0 - z(t))c_{z_{buck}}(t)\,dt \Big/ \int_0^T \delta(z_0 - z(t))dt. \tag{14}$$

The function $c(t)$ is 0 unless the trajectory reaches the absorbing boundary z_{buck} before it reaches the boundary at z_{elong}, in which case its value is 1; z_{buck} and z_{elong} are the location of the postbuckling as well as the elongated prebuckling state, respectively [37]. Hence the denominator counts the crossing events of the bead at the position z_0, whereas the numerator counts how often the trajectory hits the position z_{buck} before z_{elong} [33]. Assuming Langevin dynamics, $p_{buck}(z)$ can be used to determine the underlying 1D energy landscape $G(z)$ [33,62,63]:

$$p_{buck}(z) = \int_z^{z_{elong}} D(z')^{-1}e^{\beta G(z')}dz' \Big/ \int_{z_{buck}}^{z_{elong}} D(z')^{-1}e^{\beta G(z')}dz', \tag{15}$$

with D the diffusion coefficient and β the inverse thermal energy. Inversion and rewriting formula (15) leads to, up to

a constant,

$$G(z) = \beta^{-1}\ln\left(-D(z)\frac{dp_{\text{buck}}}{dz}\right). \tag{16}$$

Hence, the energy landscape can directly be determined from $p_{\text{buck}}(z)$. The splitting probability was calculated from the same experimental traces that were used for the deconvolution approach, with code provided by [37]. The absorbing boundaries were placed close to the peaks of the extension histograms; more precisely, z_{buck} was placed 5 nm below the histogram peak of the postbuckling state and z_{elong} 5 nm above the histogram peak of the prebuckling state. We found that the exact location of both absorbing boundaries did not change the energy landscape significantly. To reduce noise, the numerical differentiation $dp_{\text{buck}}(z)$ as well as the finally reconstructed energy barrier were smoothed with a moving average filter of 15 nm each. The filtering windows were chosen to be large enough to remove regions of locally positive slope in $dp_{\text{buck}}(z)$, such that the logarithm was undefined.

Manuel *et al.* have demonstrated that the landscape recovered with $p_{\text{buck}}(z)$ leads to the same energy landscape as for the deconvolved extension histograms, without the need of deconvolution [33]. We used the stiffness, i.e., the curvature of the energy barrier top to compare both methods. We performed a quadratic fit of an area of ± 20 nm around the top of the energy barrier and determined the curvature of the quadratic fit. For 2 pN and 320 mM NaCl we find mean curvature values of $(-2.39 \pm 0.3) \times 10^{-3} k_B T/\text{nm}^2$ and $(-2.37 \pm 0.7) \times 10^{-3} k_B T/\text{nm}^2$ for the deconvolved and splitting probability reconstructed barriers, respectively. Furthermore, the shapes of the energy landscapes overlap very well [Fig. 4(b)], and hence we conclude that both reconstruction methods give similar results to within experimental error.

For our experimental data, we found the deconvolution method to reconstruct the energy landscape to be more robust and less sensitive to smoothing than the splitting probability approach. Furthermore, the splitting probability approach can only reconstruct the energy barrier, but not the complete wells [35], e.g., it cannot determine the curvature of the minima for Kramers escape theory and hence the comparison of the attempt frequency for barrier crossing events. Therefore, we only used deconvolved histograms and the inverse Boltzmann approach for further analysis.

K. Analysis of the energy landscape and determination of the attempt rate

To calculate the attempt rate ratio between the pre- and postbuckling state $k_{\text{pre}}/k_{\text{post}}$, we applied Kramers escape theory [38,39]:

$$K = \beta D/(2\pi) \times (G''(x_{\text{min}}) \times |G''(x_{\text{max}})|)^{(1/2)} \exp(-\beta \Delta G^{\ddagger}_{\text{side}}) \tag{17}$$

with k the Kramers escape rate, $\beta = 1/k_B T$, D_x the diffusion constant, $G''(x_{\text{min}})$ the curvature at the minimum of the energy well, $G''(x_{\text{max}})$ the curvature at the maximum of the energy barrier, and $\Delta G^{\ddagger}_{\text{side}}$ the height of the energy barrier of the particular side, where "side" can be "pre" or "post" buckling state. Consequently, the ratio of the attempt rates of the pre-

and postbuckling state is

$$\frac{k_{\text{pre}}}{k_{\text{post}}} = \frac{(G''_{\text{pre}}(x_{\text{min}}))^{\frac{1}{2}}}{(G''_{\text{post}}(x_{\text{min}}))^{\frac{1}{2}}} \frac{e^{-\beta \Delta G^{\ddagger}_{\text{pre}}}}{e^{-\beta \Delta G^{\ddagger}_{\text{post}}}} \tag{18}$$

with the labels "pre" and "post" for the pre- and postbuckling state, respectively. The curvature was determined from a quadratic fit of the minimum of the energy wells that included extension information up to 20 nm to either side of the minimum.

L. Determination of the buckling equilibrium point

For several analyses, in particular for the data shown in Fig. 4, Fig. S4 [25], and Fig. 6, we analyzed the reconstructed energy landscape at the buckling equilibrium. Since we obtained extension traces in fixed steps of 0.1 turns, we used the following approach to approximate the energy landscape at $P_{\text{post}} = 0.5$: we used the data sets closest to $P_{\text{post}} = 0.5$ with $P_{\text{post}} < 0.5$ and with $P_{\text{post}} \geqslant 0.5$ and calculated the mean values of Δz_{pre}, Δz_{post}, $\Delta G^{\ddagger}_{\text{pre}}$, $\Delta G^{\ddagger}_{\text{post}}$, and the curvature, weighted by their distance to $P_{\text{post}} = 0.5$. This procedure reduced the variability and, therefore, the error bars without a significant change of the mean values compared to using only the data set closest to $P_{\text{post}} = 0.5$.

M. Reconstruction of the 2D energy landscape

The 2D energy landscape [Fig. 7(b)] was assembled from sets of 1D extension energy landscapes determined for every measured number of turns. Interpolation was performed in MATLAB (MATLAB R2013b, The MathWorks) using the "surf" and "shading interp" routines. The underlying 1D energy landscapes were aligned in the extension axis to the position of the maxima of the energy barriers to exclude errors due to tracking variability from changes in the light intensity for different rotation positions. We note that the height of the barrier was not aligned, but is determined by the analysis.

N. Impact of glycerol on the buckling transition

To further investigate the effect of friction on the observed buckling dynamics, we adjusted the viscosity of our buffer by adding varying amounts of glycerol and carried out buckling measurements for $F = 3$ pN and 100 mM NaCl. According to the model of Bai *et al.* [29], the friction should linearly affect the characteristic buckling time τ_{buck}. Importantly, the predicted effect is independent of the relative size of the friction coefficients of the bead and the DNA, since both DNA and bead friction coefficients are linear in η.

Analyzing the equilibrium properties of the buckling transition with different amounts of glycerol in the buffer, we again see essentially no dependence: ΔWr_{pre}, ΔWr_{post}, and ΔWr_b are identical, within error, for different glycerol concentrations [Fig. S5(a) [25]]. Similarly, ΔLk_b and the widths of the peaks in the extension histograms for the pre- and post-buckling states are independent of glycerol concentration [Fig. S5(b) [25]]. Only the size of the jump between the pre- and postbuckling states changes by $\sim 10\%$, decreasing from ~ 96 to ~ 86 nm upon increasing the glycerol concentration

from 0% to 35%, corresponding to an increasing of the viscosity from 0.89 to 3.2 mPa s [Fig. S5(c) [25]].

In contrast, the buckling time scale τ_{buck} changes significantly with increasing glycerol concentration [Fig. S5(e) [25]], τ_{buck} slowing down approximately $\sim$1.8-fold for an $\sim$3.5-fold increase in viscosity. While this increase is qualitatively consistent with the prediction of the model by Bai *et al.*, both the magnitude of the observed increase and its functional form deviate significantly from the model. While the Bai *et al.* model predicts a linear dependence on viscosity, the data are sublinear. Comparing the data at the lowest (buffer with no added glycerol) and highest (buffer with 35% amount glycerol) viscosities, the Bai *et al.* model significantly, by $\sim$2-fold, overpredicts the slowdown of the buckling dynamics upon increasing glycerol concentration.

The fact that the addition of glycerol slows down the buckling dynamics significantly less than would be predicted from the effect of the change in viscosity alone suggests that glycerol has other, offsetting, effects on DNA buckling. We now examine several possibilities for secondary glycerol effects and how they might explain the observed behavior: changes in the dielectric constant, crowding effects, and destabilization of the double helix.

Glycerol lowers the dielectric constant of the solution (for 35% glycerol roughly by 15%) [64] and, therefore, increases charge-charge interactions; by trend, we would expect this to have similar effects to reducing the salt concentration, which also increases charge-charge interactions by reducing screening. Lower salt concentrations result in faster hopping, i.e., they reduce τ_{buck} [Fig. 2(h)], which could explain the observed trend with glycerol. However, we note that changing salt concentration from 100 to 320 mM monovalent changes, e.g., the Debye length by roughly $\sim$2-fold, a much more pronounced effect than the at most 15% change in dielectric constant due to glycerol. If the change in charge-charge interaction would play an important role, we would also expect a change in the steady-state behavior with glycerol, as observed for different salt concentration (Fig. 2). The fact that an increase in glycerol concentration does not appear to affect the equilibrium properties of the transition [Figs. S5(a)–S5(c) [25]] suggests that the change in the dielectric constant cannot account for the observed changes in buckling behavior.

Molecular crowding can influence the characteristic time of loop formation in DNA molecules τ_{loop} [65]. In simulated DNA looping events, Shin *et al.* obtain an increase in the

characteristic looping time in the presence of small crowders, such as glycerol [65,66], for which viscosity effects dominate. In addition, in particular for larger crowders, Shin *et al.* observe an increasing in the probability of the looped compared to the unlooped state, due to caging interactions. Therefore, it appears plausible that crowding effects might stabilize the tight loop involved in the transition state, which could increase the buckling rate, in line with the observed trends. However, the effect of loop stabilization for a small crowder such as glycerol is likely to be limited. In addition, if crowding has a pronounced effect on looping, the buckling point ΔLk_b would be expected to decrease to smaller values with increasing crowding, again contrary to what is observed experimentally [Fig. S5(d) [25]], suggesting that the crowding effects of the glycerol concentrations used are relatively unimportant in our experimental situation.

Polyols, including glycerol, have been shown to destabilize the DNA helix [67]. The destabilization has been attributed to the different capability of polyhydric alcohols to interact with the polynucleotide solvation sites replacing water and to modification of the local electrostatic interactions [67]. Our results suggest that the transition state involves strong bending of the DNA and quite possibly temporary local melting. A destabilization of the helix by glycerol would facilitate melting and, therefore, would lower the transition state, thus making the hopping faster than what is expected from the viscosity only. The observed twofold faster buckling compared to the estimate from viscosity alone would only require a $\ln[2] k_B T \sim 0.7 k_B T$ reduction of the free-energy barrier, which appears plausible given the $\sim$10 °C reduction in melting temperature for calf thymus DNA over the glycerol range used in our experiments.

[1] L. F. Liu and J. C. Wang, Proc. Natl. Acad. Sci. USA **84**, 7024 (1987).

[2] N. R. Cozzarelli, G. J. Cost, M. Nollmann, T. Viard, and J. E. Stray, Nat. Rev. Mol. Cell Biol. **7**, 580 (2006).

[3] D. A. Koster, A. Crut, S. Shuman, M. A. Bjornsti, and N. H. Dekker, Cell **142**, 519 (2010).

[4] T. J. Stevens *et al.*, Nature (London) **544**, 59 (2017).

[5] F. B. Fuller, Proc. Natl. Acad. Sci. USA **75**, 3557 (1978).

[6] J. H. White, Am. J. Math. **91**, 693 (1969).

[7] A. V. Vologodskii and N. R. Cozzarelli, Annu. Rev. Biophys. Biomol. Struct. **23**, 609 (1994).

[8] T. Schlick, Curr. Opin. Struct. Biol. **5**, 245 (1995).

[9] J. Vinograd, J. Lebowitz, R. Radloff, R. Watson, and P. Laipis, Proc. Natl. Acad. Sci. USA **53**, 1104 (1965).

[10] T. R. Strick, J. F. Allemand, D. Bensimon, A. Bensimon, and V. Croquette, Science **271**, 1835 (1996).

[11] H. Brutzer, N. Luzzietti, D. Klaue, and R. Seidel, Biophys. J. **98**, 1267 (2010).

[12] J. Dekker and L. Mirny, Cell **164**, 1110 (2016).

[13] M. T. J. van Loenhout, M. V. de Grunt, and C. Dekker, Science **338**, 94 (2012).

[14] A. Crut, D. A. Koster, R. Seidel, C. H. Wiggins, and N. H. Dekker, Proc. Natl. Acad. Sci. USA **104**, 11957 (2007).

[15] J. Lipfert *et al.*, Proc. Natl. Acad. Sci. USA **111**, 15408 (2014).

[16] S. Forth, C. Deufel, M. Y. Sheinin, B. Daniels, J. P. Sethna, and M. D. Wang, Phys. Rev. Lett. **100**, 148301 (2008).

[17] B. C. Daniels and J. P. Sethna, Phys. Rev. E **83**, 041924 (2011).

[18] L. Postow, C. D. Hardy, J. Arsuaga, and N. R. Cozzarelli, Genes Dev. **18**, 1766 (2004).

[19] J. Lipfert, X. Hao, and N. H. Dekker, Biophys. J. **96**, 5040 (2009).

[20] B. M. Lansdorp and O. A. Saleh, Rev. Sci. Instrum. **83**, 025115 (2012).

[21] J. F. Allemand, D. Bensimon, R. Lavery, and V. Croquette, Proc. Natl. Acad. Sci. USA **95**, 14152 (1998).

[22] B. M. Lansdorp, S. J. Tabrizi, A. Dittmore, and O. A. Saleh, Rev. Sci. Instrum. **84**, 044301 (2013).

[23] A. Huhle, D. Klaue, H. Brutzer, P. Daldrop, S. Joo, O. Otto, U. F. Keyser, and R. Seidel, Nat. Commun. **6**, 5885 (2015).

[24] D. Dulin, T. J. Cui, J. Cnossen, M. W. Docter, J. Lipfert, and N. H. Dekker, Biophys. J. **109**, 2113 (2015).

[25] See Supplemental Material at http://link.aps.org/supplemental/10.1103/PhysRevE.98.042412 for material and methods as well as detailed analysis.

[26] P. Daldrop, H. Brutzer, A. Huhle, D. J. Kauert, and R. Seidel, Biophys. J. **108**, 2550 (2015).

[27] J. D. Moroz and P. Nelson, Proc. Natl. Acad. Sci. USA **94**, 14418 (1997).

[28] J. Lipfert, J. W. Kerssemakers, T. Jager, and N. H. Dekker, Nat. Methods **7**, 977 (2010).

[29] H. Bai, J. E. Kath, F. M. Zorgiebel, M. Sun, P. Ghosh, G. F. Hatfull, N. D. Grindley, and J. F. Marko, Proc. Natl. Acad. Sci. USA **109**, 16546 (2012).

[30] J. Lipfert, M. M. van Oene, M. Lee, F. Pedaci, and N. H. Dekker, Chem. Rev. **115**, 1449 (2015).

[31] J. C. Meiners and S. R. Quake, Phys. Rev. Lett. **84**, 5014 (2000).

[32] M. T. Woodside, P. C. Anthony, W. M. Behnke-Parks, K. Larizadeh, D. Herschlag, and S. M. Block, Science **314**, 1001 (2006).

[33] M. T. Woodside and S. M. Block, Annu. Rev. Biophys. **43**, 19 (2014).

[34] P. A. Jansson, *Deconvolution of Images and Spectra*, 2nd ed. (Academic, San Diego, 1996).

[35] A. P. Manuel, J. Lambert, and M. T. Woodside, Proc. Natl. Acad. Sci. USA **112**, 7183 (2015).

[36] R. Du, V. S. Pande, A. Y. Grosberg, T. Tanaka, and E. S. Shakhnovich, J. Chem. Phys. **108**, 334 (1998).

[37] J. D. Chodera and V. S. Pande, Phys. Rev. Lett. **107**, 098102 (2011).

[38] H. A. Kramers, Physica **7**, 284 (1940).

[39] P. Hänggi, P. Talkner, and M. Borkovec, Rev. Mod. Phys. **62**, 251 (1990).

[40] R. Berkovich, R. I. Hermans, I. Popa, G. Stirnemann, S. Garcia-Manyes, B. J. Berne, and J. M. Fernandez, Proc. Natl. Acad. Sci. USA **109**, 14416 (2012).

[41] H. Lannon, J. S. Haghpanah, J. K. Montclare, E. Vanden-Eijnden, and J. Brujic, Phys. Rev. Lett. **110**, 128301 (2013).

[42] J. Leach, H. Mushfique, S. Keen, R. Di Leonardo, G. Ruocco, J. M. Cooper, and M. J. Padgett, Phys. Rev. E **79**, 026301 (2009).

[43] H. Faxén, Ann. Phys. **373**, 89 (1922).

[44] M. A. Catipovic, P. M. Tyler, J. G. Trapani, and A. R. Carter, Am. J. Phys. **81**, 485 (2013).

[45] E. Stellwagen and N. C. Stellwagen, Anal. Chem. **87**, 9042 (2015).

[46] B. Sudhanshu, S. Mihardja, E. F. Koslover, S. Mehraeen, C. Bustamante, and A. J. Spakowitz, Proc. Natl. Acad. Sci. USA **108**, 1885 (2011).

[47] T. A. Lionberger, D. Demurtas, G. Witz, J. Dorier, T. Lillian, E. Meyhofer, and A. Stasiak, Nucl. Acids Res. **39**, 9820 (2011).

[48] T. R. Strick, V. Croquette, and D. Bensimon, Proc. Natl. Acad. Sci. USA **95**, 10579 (1998).

[49] C. Matek, T. E. Ouldridge, J. P. Doye, and A. A. Louis, Sci. Rep. **5**, 7655 (2015).

[50] R. N. Irobalieva *et al.*, Nat. Commun. **6**, 8440 (2015).

[51] J. S. Mitchell, C. A. Laughton, and S. A. Harris, Nucl. Acids Res. **39**, 3928 (2011).

[52] A. Dittmore, S. Brahmachari, Y. Takagi, J. F. Marko, and K. C. Neuman, Phys. Rev. Lett. **119**, 147801 (2017).

[53] J. F. Marko and S. Neukirch, Phys. Rev. E **85**, 011908 (2012).

[54] O. K. Dudko, G. Hummer, and A. Szabo, Proc. Natl. Acad. Sci. USA **105**, 15755 (2008).

[55] Y. Suzuki and O. K. Dudko, Phys. Rev. Lett. **104**, 048101 (2010).

[56] D. A. Koster, K. Palle, E. S. Bot, M. A. Bjornsti, and N. H. Dekker, Nature (London) **448**, 213 (2007).

[57] J. P. Cnossen, D. Dulin, and N. H. Dekker, Rev. Sci. Instrum. **85**, 103712 (2014).

[58] A. J. te Velthuis, J. W. Kerssemakers, J. Lipfert, and N. H. Dekker, Biophys. J. **99**, 1292 (2010).

[59] C. Bouchiat, M. D. Wang, J. Allemand, T. Strick, S. M. Block, and V. Croquette, Biophys. J. **76**, 409 (1999).

[60] R. K. Milne, G. F. Yeo, B. W. Madsen, and R. O. Edeson, Biophys. J. **55**, 673 (1989).

[61] D. R. Burnham, I. De Vlaminck, T. Henighan, and C. Dekker, PloS One **9**, e108271 (2014).

[62] Y. M. Rhee and V. S. Pande, J. Phys. Chem. B **109**, 6780 (2005).

[63] R. B. Best and G. Hummer, Proc. Natl. Acad. Sci. USA **107**, 1088 (2010).

[64] A. Glycerine Producers, *Physical Properties of Glycerine and Its Solutions* (Glycerine Producers' Association, New York, 1963).

[65] J. Shin, A. G. Cherstvy, and R. Metzler, Soft Matter **11**, 472 (2015).

[66] K. Kiyosawa, Biochim. Biophys. Acta **1064**, 251 (1991).

[67] P. Del Vecchio, D. Esposito, L. Ricchi, and G. Barone, Int. J. Biol. Macromol. **24**, 361 (1999).